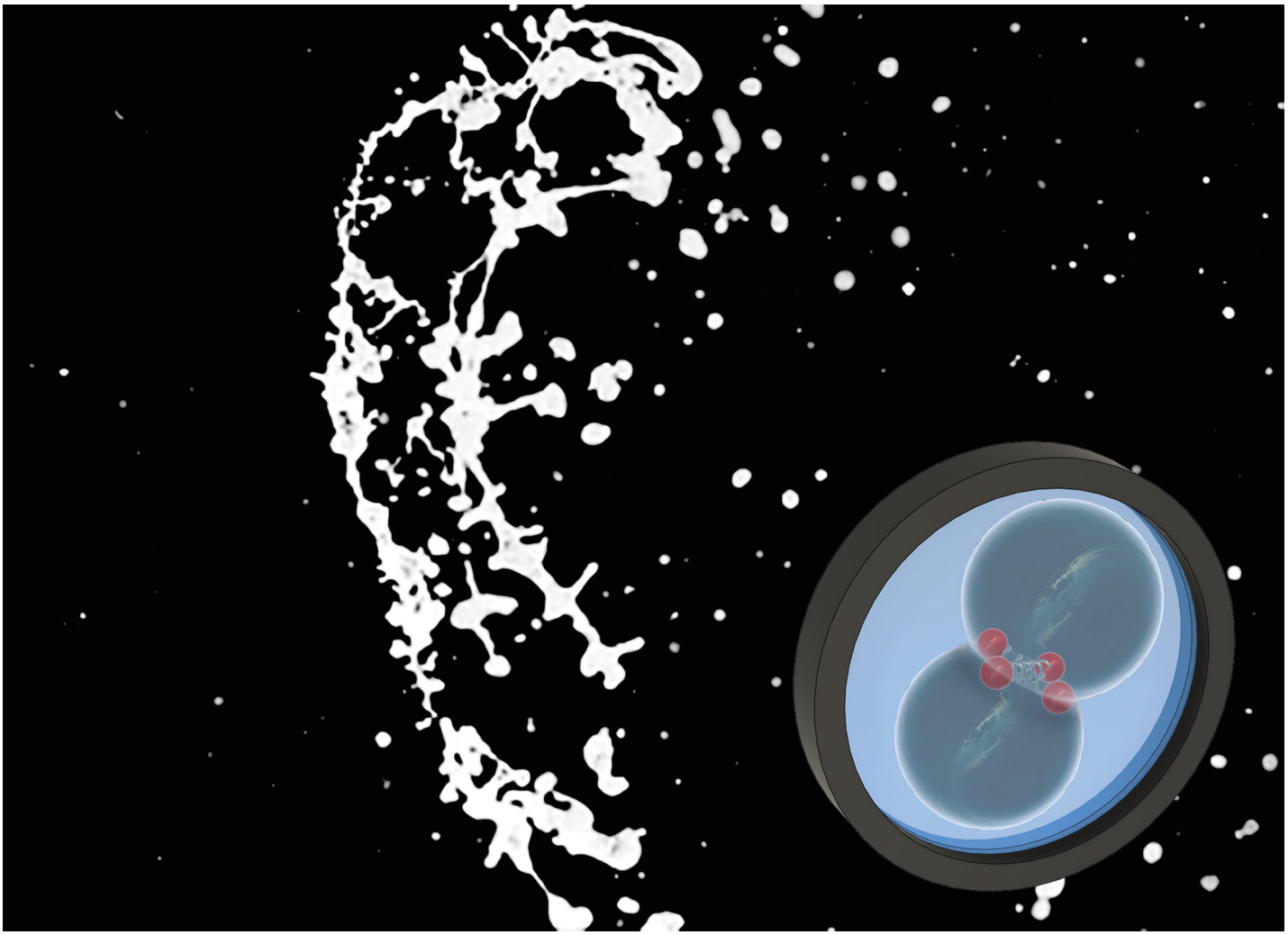

Highlighting research from Professor Aloke Kumar's lab at the Indian Institute of Science, Bangalore.

Sub-Newtonian coalescence in polymeric fluids

When fluid droplets come in contact, they tend to coalesce and achieve a lower energy state. We study the coalescence of droplets of polymeric fluids and observe that their coalescence proceeds at slower rates as compared to the corresponding regime of Newtonian fluid droplets coalescence. Since the coalescence shows a slower power-law behavior, we term this coalescence as sub-Newtonian coalescence.

Image credit: Kumar Lab

As featured in:

See Aloke Kumar *et al.*, *Soft Matter*, 2023, **19**, 4847.

ROYAL SOCIETY OF CHEMISTRY

rsc.li/soft-matter-journal

Registered charity number: 207890

Soft Matter

PAPER

View Article Online
View Journal | View Issue

Cite this: *Soft Matter*, 2023, **19**, 4847

Sub-Newtonian coalescence in polymeric fluids†

Abhineet Singh Rajput, Sarath Chandra Varma and Aloke Kumar *

Received 18th January 2023,
Accepted 30th May 2023

DOI: 10.1039/d3sm00069a

rsc.li/soft-matter-journal

We present a theoretical framework for capturing the coalescence of a pendant drop with a sessile drop in polymeric fluids. The framework is based on the unification of various constitutive laws under a high Weissenberg creeping flow limit. Our results suggest that the phenomenon comes under a new regime, namely, the sub-Newtonian regime followed by the limiting case of arrested coalescence with the arrest angle $\theta_{arrest} \propto Ec_{-1}^{-1/2}$, where Ec_{-1} is the inverse of Elasto-capillary number. Furthermore, we propose a new time scale T^* integrating the continuum variable Ec_{-1} and the macromolecular parameter N_e, the entanglement density to describe the liquid neck evolution. Finally, we validate the framework with high-speed imaging experiments performed across different molecular weights of poly(ethylene oxide) (PEO).

1. Introduction

Coalescence is an energy minimization phenomenon in which two drops merge to form a thermodynamically stable daughter drop.[1] Coalescence of droplets of Newtonian fluids plays a key role in raindrop condensation,[2,3] combustion,[4] and atomization of metal droplets;[5] while non-Newtonian fluid droplet coalescence finds applications in the food industry,[6] spray coating and paintings,[7,8] and even processes linked to life like those in the growth and development of tumors.[9] Despite the varied and versatile application of non-Newtonian fluids, coalescence dynamics of such fluids remain a sparsely studied area. The vastness of the domain of non-Newtonian fluids – they can range from macromolecular fluids to various colloids – makes a unified understanding even more elusive. Each subclass has a different micro-structure composition leading to distinct behaviors. However, there are few recent studies on a special class of non-Newtonian fluids *i.e.*, macromolecular fluids[10–14] that have highlighted the deviation from proposed Newtonian behaviour. But a generalized theoretical framework unifying various constitutive laws to probe the phenomenon in viscoelastic droplets remains an open question.

A recent study by Chen *et al.*[14] on polymers and gels showed that at later time scales, coalescence is slower than in Newtonian droplets. This conclusion was drawn based on stress relaxation behaviour observed in polymers using molecular dynamics simulation. Similarly, Xu *et al.*[15] also reported slower growth of the neck during the coalescence of two immiscible Newtonian droplets. Another study, which employed numerical experiments on sessile–sessile drop coalescence of power-law fluids, showed a deviation from Newtonian behaviour as a function of the power-law exponent.[16] Our previous study on polymeric droplet coalescence[12] highlighted the relevance of macromolecular relaxation time on the neck radius evolution R. Instead of viscous *versus* inertial regime delineation in Newtonian fluids, aqueous solutions of macromolecules showed three different regimes namely, inertio-elastic, viscoelastic, and elasticity dominated regimes. The non-dimensional parameter concentration ratio, c/c^*, governed the appearance of the various regimes. It has also been shown that the temporal evolution of the bridge follows a universal behaviour in inertio-elastic and viscoelastic regimes *i.e.*, $R \sim t^b$ (where b is the power-law exponent) with $b = 0.37$ along with continuously decreasing b in the elasticity dominated regime. Based on scaling analysis using linear Phan–Thein–Tanner (PTT)[17,18] constitutive equation the study proposed a time scale $\tau^* = \sqrt{\frac{\eta_0\lambda}{\rho R_0^2}}$ where η_0, ρ, R_0 and λ are the viscosity, density, length scale of the polymeric droplet and relaxation time of the polymeric solution, respectively. Whether these deviations from Newtonian behaviour in macromolecular fluids is purely due to viscoelasticity or there exists contribution from shear rate dependent viscosity remains unresolved. Recently, Fardin *et al.*[19] showed the similarity between spreading, pinching and coalescence for Newtonian fluids using Ohensorge units. But, for macromolecular fluids like polymer solutions, even the slight addition of the polymer to solvent alters the breakup dynamics drastically compared to its Newtonian counterpart. It is also worthwhile to note that the experimental methodology can play a key role in determining the coalescence kinetics. For example, one method to trigger coalescence can be to pump fluid into a droplet, thereby increasing its volume,

Department of Mechanical Engineering, Indian Institute of Science, Bangalore, India. E-mail: alokekumar@iisc.ac.in

† Electronic supplementary information (ESI) available. See DOI: https://doi.org/10.1039/d3sm00069a

till coalescence with a nearby droplet is achieved. Dekker *et al.*[20] used this method to demonstrate that coalescence of a polymeric fluid results in bridge evolution dynamics similar to Newtonian fluids. However, Varma *et al.*[13] later showed that coalescence signatures are affected by the experimental methodology chosen. Specifically, they demonstrated that for the sessile–sessile configuration the coalescence triggered *via* the volume filling method (VFM) results in Newtonian-like bridge evolution dynamics, whereas in the droplet spreading method (DSM), it deviates from the Newtonian behavior for the same concentrations of polymers. It is likely that as this field of work evolves, a coherence and standardization of experimental methodologies will occur.

In the current study, we have developed a theoretical model to capture the neck radius evolution across different regimes. The theoretical framework is developed based on the unification of Oldroyd-B, linear PTT, Gesikus constitutive equations[21] under high Weissenberg number Wi creeping flow limit. However, for simplicity we use the Giesekus constitutive equation[22] to explain the model. The proposed model is validated with the experiments performed with poly(ethylene oxide) (PEO) for a range of molecular weights M_w. Apart from the theoretical model, we have also demonstrated the effect of entanglement density N_e on the coalescence to propose a new time scale T^* that intertwines continuum and molecular approaches to macromolecular fluid. Using the analogy of sub-diffusive behavior in Brownian dynamics, we name this broader class of sluggish merging of two droplets as sub-Newtonian coalescence. For the sessile-pendant droplet configuration, the regime of sub-Newtonian coalescence is marked by a power-law exponent b such that $0 < b < 0.5$. The right-hand limit corresponds to a purely viscous Newtonian fluid, whereas the left-hand limit corresponds to arrested-coalescence. Macromolecular fluids coalescence is an example of sub-Newtonian coalescence where the presence of an additional resistance by elastic force slows down the coalescence resulting in an exponent b lesser than the universal $b = 0.5$ for Newtonian fluids. Even in Newtonian droplet coalescence, if the drops are immiscible one may see a sub-Newtonian coalescence.[15] Furthermore we also propose a theoretical limit for an arrested coalescence ($b \to 0$). A regime map delineating the Newtonian ($b = 0.5$) represented as black dashed line, sub-Newtonian ($b < 0.5$) and the arrested coalescence ($b \to 0$) is shown in Fig. 1 with the blue dashed line representing the universality proposed for the polymeric fluids in our previous study[10] and the solid red line signifying the arrested limit. It can be observed from Fig. 1 that the neck evolution slows down as one moves from a Newtonian to a sub-Newtonian regime with the limiting case being the arrested coalescence. A detailed discussion on arrested coalescence is presented in the later sections.

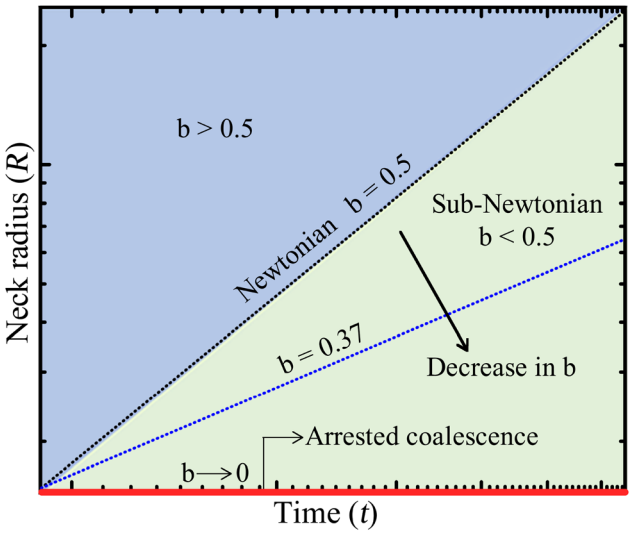

Fig. 1 Regime map showing the classification of coalescence based on power-law exponent b.

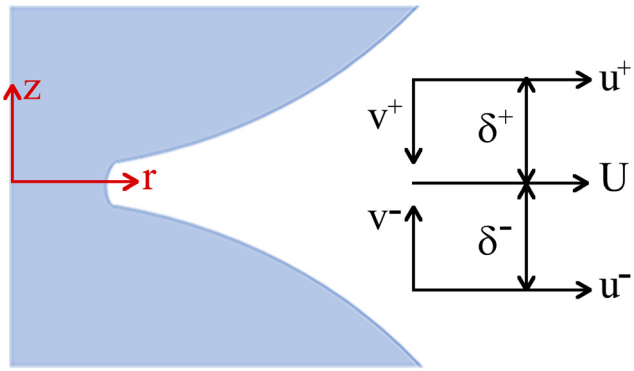

Fig. 2 Schematic of velocity distribution at the neck region for sessile-pendant coalescence.

2. Theory

To obtain the theoretical solution for the coalescence phenomenon, we utilize the symmetry of the problem and formulate our analysis in cylindrical coordinates as shown in Fig. 2. The kinematics of the flow $(u_r, u_z) := (u,v)$ is assumed to be quasi-radial at the neck region $z = 0$ implying that $u \neq 0$ and $v = 0$. For a small region of width δ on either side of the $z = 0$ line the flow field is such that $u^+ = u^- \neq 0$ and $v^+ = -v^- \neq 0$, respectively. Using mirror symmetry and quasi-radial assumptions, the flow field at the $z = 0$ line has the constraints of $\frac{\partial u}{\partial z} = 0$ and $\frac{\partial v}{\partial r} = 0$.

The dynamics of the coalescence phenomenon is governed by conservation of mass and momentum equations along the $z = 0$ line as shown in eqn (1) and (2). To get components of stress tensor τ in eqn (2) we employ the Giesekus constitutive equation represented in eqn (3).

$$\frac{\partial u}{\partial r} + \frac{\partial v}{\partial z} + \frac{u}{r} = 0 \tag{1}$$

$$\rho\left(u\frac{\partial u}{\partial r}\right) = -\frac{\partial p}{\partial r} + \frac{\partial \tau_{rr}}{\partial r} + \frac{\tau_{rr}}{r} + \frac{\partial \tau_{rz}}{\partial z} \tag{2}$$

$$\boldsymbol{\tau} + \lambda \overset{\nabla}{\boldsymbol{\tau}} + \frac{\alpha\lambda}{\eta_0}\boldsymbol{\tau}\boldsymbol{\tau} = 2\eta_0\mathbf{D} \tag{3}$$

where, $\overset{\nabla}{\boldsymbol{\tau}} = \frac{\partial \boldsymbol{\tau}}{\partial t} + \mathbf{v}.\nabla\boldsymbol{\tau} - (\nabla\mathbf{v})\boldsymbol{\tau} - \boldsymbol{\tau}(\nabla\mathbf{v})^T$ is the upper convected derivative, $\mathbf{D}$ is the rate of deformation tensor, α is the model parameter, and η_0 and λ are the zero shear viscosity and fluid relaxation time respectively.

By introducing the non-dimensional variables: $\mathrm{v}^* = \mathrm{v}/U_c$, $r^* = r/L$, $z^* = z/L$, $t^* = t/T$, $\boldsymbol{\tau}^* = \boldsymbol{\tau}/\boldsymbol{\tau}_c$, where $\mathbf{v}$, $T := L/U_c$, U_c, L, $\boldsymbol{\tau}_c$ are the velocity vector, characteristic time, characteristic velocity, characteristic length, and characteristic stress respectively into eqn (1)–(3) we obtain their dimensionless forms. The dimensionless form of the Giesekus constitutive equation is represented in eqn (4).

$$\tau_c\boldsymbol{\tau}^* + \frac{\tau_c\lambda U_c}{L}\left(\frac{\partial \boldsymbol{\tau}^*}{\partial t^*} + \overset{\nabla}{\boldsymbol{\tau}}* + \frac{\alpha\tau_c L}{\eta_0 U_c}\boldsymbol{\tau}^*\boldsymbol{\tau}^*\right) = 2\frac{\eta_0 U_c}{L}\mathbf{D}^* \tag{4}$$

Linear PTT equivalent of eqn (4) is reduced to different forms as proposed in the literature.[10,12] Based on the dominant scale of $\boldsymbol{\tau}_c$ the constitutive law can be reduced into three distinct regimes when $U_c = U$ (U is neck velocity), namely the viscous dominant regime $\left(\boldsymbol{\tau}_c = \frac{\eta_0 U}{L}\right)$ and viscoelastic regime $\left(\boldsymbol{\tau}_c = \mathrm{Wi}\frac{\eta_0 U}{L}\right)$ where, $\mathrm{Wi} = \frac{\lambda U}{L}$ is the Weissenberg number and in the elasticity dominant regime $\left(\boldsymbol{\tau}_c = \frac{\eta_0}{\lambda}\right)$. Recently Varma *et al.*[12] used the scale $\left(\boldsymbol{\tau}_c = \frac{\eta_0}{\lambda}\right)$ in the elasticity dominated regime to predict the behaviour of b during coalescence. For inertio-elastic and viscoelastic regimes a semi-analytical model is proposed by Varma *et al.*[10] in which the upper convected derivative in eqn (4) was dropped under the limit of High Re low Wi with the approximations of $\lambda\mathrm{Wi}^2 \ll 1$. However, that approximation is not valid in the elasticity dominated regime as the Reynolds number $\mathrm{Re} = \frac{\rho U L}{\eta_0}$ is $\mathcal{O}(10^{-5})$ and Weissenberg number Wi is $\mathcal{O}(10^3)$ as shown in our previous study[12] indicating that the flow has low Re and high Wi. A detailed discussion on the Re and Wi for the present study is given in the Results and discussion section. For low Re and high Wi flows, the upper convective derivative of stress in the constitutive equation is the dominant term in eqn (4) (see the ESI† for the detailed derivation). Similarly, Renardy[23] showed that the upper convected derivative in the various constitutive equations[21] like Maxwell, Oldroyd-B, Linear PTT, and exponential PTT model is the dominant term under quasi-steady assumption at high Wi and low Re. As the upper convective derivative is the predominant term, the present theory unifies these continuum based constitutive equations to eqn (5). However, for the coalescence of two sessile polymeric drops,[13] a theoretical model which is independent of characteristic stresses has been proposed for viscoelastic and elasticity dominated regimes using thin film lubrication approximation.

$$\overset{\nabla}{\boldsymbol{\tau}}* = 2\mathbf{D}^* \tag{5}$$

As the coalescence phenomenon is predominately extensional,[24] both the upper and lower convected derivative can be used to model the physics.[25] In the present analysis, we have used the lower convected derivative $\overset{\Delta}{\boldsymbol{\tau}}* = \frac{\partial \boldsymbol{\tau}}{\partial t} + \mathbf{v}\cdot\nabla\boldsymbol{\tau} + (\nabla\mathbf{v})\boldsymbol{\tau} + \boldsymbol{\tau}(\nabla\mathbf{v})^T$. For capturing the neck evolution dynamics, the stress tensor in eqn (5) is simplified for the spatial region $z = 0$ under the quasi-steady and quasi-radial assumptions by introducing the dimensionless variables ($u^* = u/U_c$, $r^* = r/L$, $z^* = z/Z_c$, $t^* = t/T_c$, $\tau^*_{rr} = \tau_{rr}/\tau_{rc}$ and $\tau^*_{rz} = \tau_{rz}/\tau_{zc}$, where $T_c := L/U_c$, U_c, $L = R_0$, $Z_c = L^2/2R_0$, τ_{rc} and τ_{zc} are the characteristic time, velocity, lengths and stresses respectively and R_0 is the droplet radius. Here $U_c := \sqrt{\eta_0/\rho\lambda}$ is the shear wave velocity, $\tau_{rc} = \eta_0/\lambda$ is the shear modulus, $Z_c = R_0/2$, $\tau_{zc} := \tau_{rc}/\mathrm{Wi}_c$ with $\mathrm{Wi}_c = \lambda U_c/R_0$ as the characteristic Weissenberg number, and $P_c = \sigma/R_0$ is the characteristic pressure) to eqn (6a) and (6b). The individual dimensionless components of stress tensor as represented in eqn (7a) and (7b) are obtained by integrating eqn (6a) and (6b) along the $z = 0$ line.

$$u^*\frac{\partial \tau^*_{rr}}{\partial r^*} + 2\tau^*_{rr}\frac{\partial u^*}{\partial r^*} = 2\frac{\partial u^*}{\partial r^*} \tag{6a}$$

$$u^*\frac{\partial \tau^*_{rz}}{\partial r^*} - u^*\frac{\tau^*_{rz}}{r^*} = 0 \tag{6b}$$

$$\tau^*_{rr} = 1 + K_1/(u^*)^2 \tag{7a}$$

$$\tau^*_{rz} = K_2 r^* \tag{7b}$$

Here, K_1 and K_2 are dimensionless integrating constants which in general are functions of z locally. Furthermore, the radial momentum equation is simplified to obtain:

$$\left(\frac{\rho U_c^2}{R_0}\right)u^*\frac{\partial u^*}{\partial r^*} = -\frac{P_c}{R_0}\frac{\partial p^*}{\partial r^*} + \frac{\tau_{rc}}{R_0}\left(\frac{\partial \tau^*_{rr}}{\partial r^*} + \frac{\tau^*_{rr}}{r^*}\right) + \frac{\tau_{zc}}{Z_c}\frac{\partial \tau^*_{rz}}{\partial z^*} \tag{8}$$

To get the semi-analytical solution for the neck evolution, the dimensionless momentum eqn (8) is further simplified to eqn (9) by introducing the scaling arguments $r^* \sim R^* = R/R_0$, $z^* \sim Z^* = (R/R_0)^2$, $u^* \sim U^* = U/U_c$ (Note: R and U are the temporal neck radius and neck evolution speed respectively) along with the terms from the stress tensor as $\frac{\partial \tau^*_{rr}}{\partial r^*} \sim \frac{\tau^*_{rr}}{R^*}$, and $\frac{\partial p^*}{\partial r^*} \sim \frac{p^*}{R*}$ with $p^* = \left(\frac{1}{R^*} + \frac{2}{(R^*)^2}\right)$.[12] Here, eqn (9) is a bi-quadratic equation of the form given in eqn (10) with M_1, M_2 and M_3 as scaling constants. Eqn (10) has 4 solutions in which two are negative and two are positive. However, the negative solutions are physically irrelevant as they suggest the neck collapses with time. Among the two acceptable solutions $\sqrt{\frac{P}{2} + \sqrt{\frac{P^2}{4} + Q}}$ captures the physical scenario. Therefore, the acceptable solution of eqn (10) is of the form eqn (11) where $U^* = \frac{\mathrm{d}R^*}{\mathrm{d}t^*}$ and $P(M_1, M_2, M_3, R^*, \mathrm{Wi}_c) := \left(M_1\left(\frac{1}{R^*} + \frac{2}{(R^*)^2}\right) + M_2 + \frac{2M_3}{\mathrm{Wi}_c}\right)$ (see the ESI† for the detailed

derivation).

$$(U^*)^4 - \left(M_1\left(\frac{1}{R^*} + \frac{2}{(R^*)^2}\right) + M_2 + \frac{2M_3}{\mathrm{Wi_c}}\right)(U^*)^2 - M_2 = 0 \quad (9)$$

$$(U^*)^4 - P(M_1, M_2, M_3, R^*, \mathrm{Wi_c})(U^*)^2 - M_2 = 0 \quad (10)$$

$$\frac{\mathrm{d}R^*}{\mathrm{d}t^*} = \sqrt{\frac{P}{2} + \sqrt{\frac{P^2}{4} + M_2}} \quad (11)$$

Eqn (11) is solved using a first order finite difference scheme, in which time step Δt is taken to be sufficiently small to ensure numerical stability. The solution of eqn (11) is validated with experiments. The details of the experiments are provided in the next section.

3. Materials and methods

Poly(ethylene oxide) (PEO) of molecular weight $M_w = 6 \times 10^5$ and 1×10^5 g mol^{-1}, solutions of various concentrations c are prepared by adding the sufficient quantity of polymer to DI Water. All the solutions are agitated at 300 rpm to ensure homogeneous dispersion. Concentrations are chosen such that the solutions are in a semi-dilute entangled regime ($c > c_e$, where $c_e = 6c^*$[26] is an entanglement concentration and c^* is the critical concentration). The critical concentration is obtained using the Mark–Houwink–Sakurada relationship[27] for PEO and Flory relationship $c^* = \frac{1}{0.072M_w^{0.65}}$. For $M_w = 4 \times 10^6$ and 5×10^6 g mol^{-1} the data is taken from our previous study.[12] The concentrations and corresponding concentration ratios c/c^* of the solutions are given in Table 1 along with the Ohnesorge number $\mathrm{Oh_o} = \frac{\eta_0}{\sqrt{\rho\sigma R_0}}$ and scaled relaxation time[12] $\tau^* = \sqrt{\frac{\eta_0\lambda}{\rho R_0^2}}$ and the rheology data in Fig. 3. The details of the relaxation time calculations are given in the ESI.†

Experiments are performed on a glass substrate coated with Polydimethylsiloxane (PDMS). Before coating the PDMS, substrates are cleansed with detergent followed by sonication with DI water and acetone for 20 min each and later allowing them to dry in a hot air oven at 95 °C for 30 min. PDMS and the curing agent (Syl Gard 184 Silicone Elastomer Kit, Dow Corning) are mixed in 1 : 10 ratio through agitation. This mixture is desiccated for 30 min to remove the visible bubbles

Table 1 Rheological properties of the solutions and power law index b and b_{theo} for neck evolution $R = at^b$ across different concentration ratios across molecular weights g mol^{-1}

M_w (g mol^{-1})	c (% w/v)	c/c^*	b	b_{theo}	η_0 (Pa s)	λ (ms)	$G = \frac{\eta_0}{\lambda}$(Pa)	$\mathrm{Oh_o}$	τ^a	m_1
1×10^5	20.0	25.61	0.31	0.31	0.82	1.7	474	3.3	1.2	450
	22.5	28.81	0.27	0.28	1.42	2.2	643	5.7	1.8	290
	25.0	32.01	0.24	0.25	1.88	2.8	684	7.6	2.3	160
	27.5	35.21	0.22	0.23	3.00	3.4	896	12	3.2	180
	30.0	38.41	0.19	0.19	3.92	4.0	978	16	4	110
	35.0	44.81	0.17	0.17	7.96	5.6	1432	32	6.7	120
6×10^5	1.5	6.16	0.41	0.42	0.035	1.7	21	0.14	0.24	1600
	3.0	12.31	0.40	0.41	0.23	7.3	32	0.9	1.3	1290
	4.5	18.47	0.32	0.33	1.20	16.9	71	4.8	4.5	520
	6.0	24.62	0.23	0.24	3.00	30.7	98	12	9.6	180
	7.5	30.78	0.22	0.23	13.00	48.7	267	52	25	240
	9.0	36.93	0.16	0.17	30.30	71.1	426	122	46	120
4×10^{6a}	0.5	7.04	0.39	0.40	0.038	58	0.66	0.14	1.2	100
	1.0	14.08	0.39	0.40	0.6	250	2.4	2.2	10	250
	1.5	21.13	0.38	0.39	2	570	3.5	7.3	28	280
	2.0	28.17	0.35	0.37	10	1040	9.6	37	85	195
	2.5	35.21	0.31	0.32	16	1650	9.7	59	135	88
	3.0	42.25	0.24	0.25	75	2400	31	275	354	100
5×10^{6a}	0.1	1.64	0.39	0.40	0.006	1.7	3.5	0.02	0.08	290
	0.2	3.28	0.39	0.40	0.018	2.5	7.2	0.07	0.18	590
	0.4	6.56	0.38	0.40	0.06	42	1.4	0.22	1.3	70
	0.75	12.29	0.36	0.37	0.8	165	4.8	2.9	9.6	230
	1	16.39	0.37	0.39	4.5	500	9	16	40	700
	1.5	24.59	0.31	0.32	20	670	30	73	96	450
	1.75	28.68	0.28	0.29	40	1325	30	147	192	450
	2.25	36.88	0.24	0.24	72	1430	50	264	267	210
	2.5	40.98	0.22	0.23	85	1590	53	312	306	145
	2.75	45.08	0.20	0.20	190	2000	95	697	514	210
	3	49.18	0.17	0.17	210	2250	93	770	573	95
	3.25	53.28	0.16	0.16	230	2500	92	843	632	68

[a] Represents data obtained from Varma *et al.*[12]

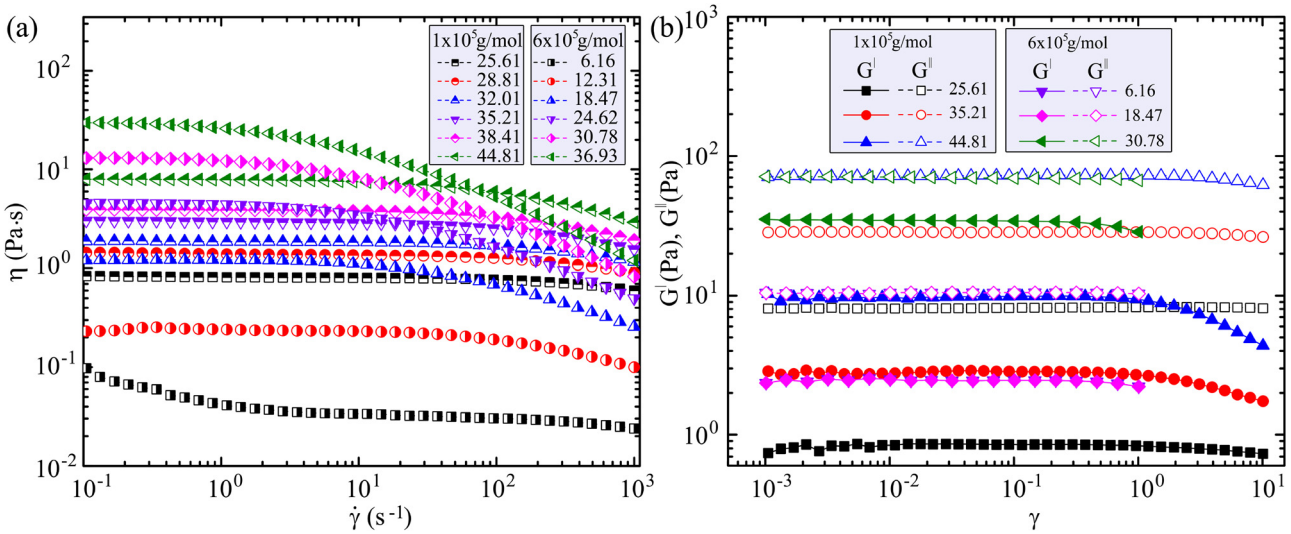

Fig. 3 Rheological behavior of PEO M_w = 1 × 10^5 g mol^{-1} and M_w = 6 × 10^5 g mol^{-1}. (a) Variation of viscosity with shear rate for different concentration ratios. (b) Variation of the storage modulus G' and the loss modulus G'' with shear strain from amplitude sweep experiments for various c/c^* (standard deviation of the data is less than 2% for all the concentrations).

in the solution. Finally, the PDMS substrates are obtained by dripping the mixture on a glass substrate and spin coating at 5000 rpm for 60 s. A sessile drop is obtained by dispensing a drop of volume 7.5 μL on a substrate. Coalescence is achieved by bringing a sessile drop of the same volume towards the pendant drop at an approach velocity of 10^{-4} m s^{-1}. A schematic of the experimental setup is shown in Fig. 4(a). A high speed camera (Photron Fastcam mini) with a Navitar lens attachment is used to capture the coalescence phenomenon at 170 000 fps. Image processing is performed on MATLAB using the custom algorithms. Validation of the experimental setup was achieved with DI Water, as represented in Fig. S1 (ESI†).

4. Results and discussion

Once the droplets touch each other, the neck begins to grow to attain the thermodynamic equilibrium state of a single daughter droplet. This neck growth is characterised by the temporal evolution of neck radius R and semi-bridge height H as represented in Fig. 4(a). These evolutions of neck radius at different time instants for DI water, c/c^* = 16.39 of PEO M_w = 5 × 10^6 g mol^{-1}, c/c^* = 12.31 and c/c^* = 24.62 of PEO M_w = 6 × 10^5 g mol^{-1} are shown in Fig. 4(b) respectively. The neck radius evolution for various concentration ratios of M_w = 1 × 10^5 and 6 × 10^5 g mol^{-1} is shown in Fig. 5(a). The data represented for all the concentration ratios is of an average of 5 trials. It can be observed from Fig. 5(a) that the neck radius evolution follows a power-law behaviour[10] $R = at^b$ in the region of interest (ROI) along with a decrease in power-law exponent b with c/c^* which is consistent with our previous study.[12] The error in measurement of b is less than ±5%. The accuracy of the fit for c/c^* = 18.47, 25.61 for three experimental trials is shown in Fig. S2 (ESI†) as a representation.

Region of interest (ROI)

The region of interest (ROI) in the present study corresponds to the linear portion of the initial neck growth. At the onset of

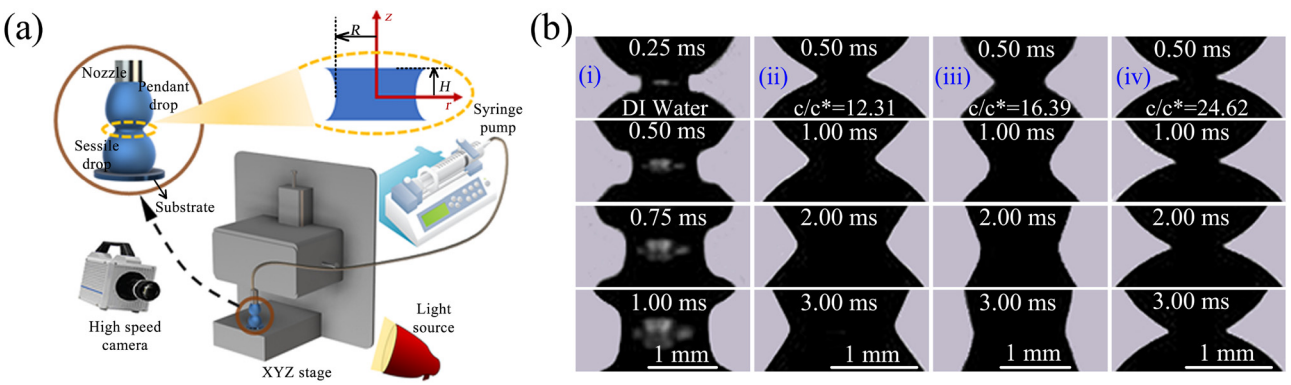

Fig. 4 (a) Schematic of the experimental setup showing the geometric parameters neck radius R and semi-bridge height H. (b) Snapshots showing the neck at different time instants for (i) DI water, (ii) c/c^* = 12.31 of PEO M_w = 6 × 10^5 g mol^{-1} and (iii) c/c^* = 16.39 of PEO M_w = 5 × 10^6 g mol^{-1}, and (iv) c/c^* = 24.62 of PEO M_w = 6 × 10^5 g mol^{-1} (note: snapshots for arrested coalescence are given in a later section).

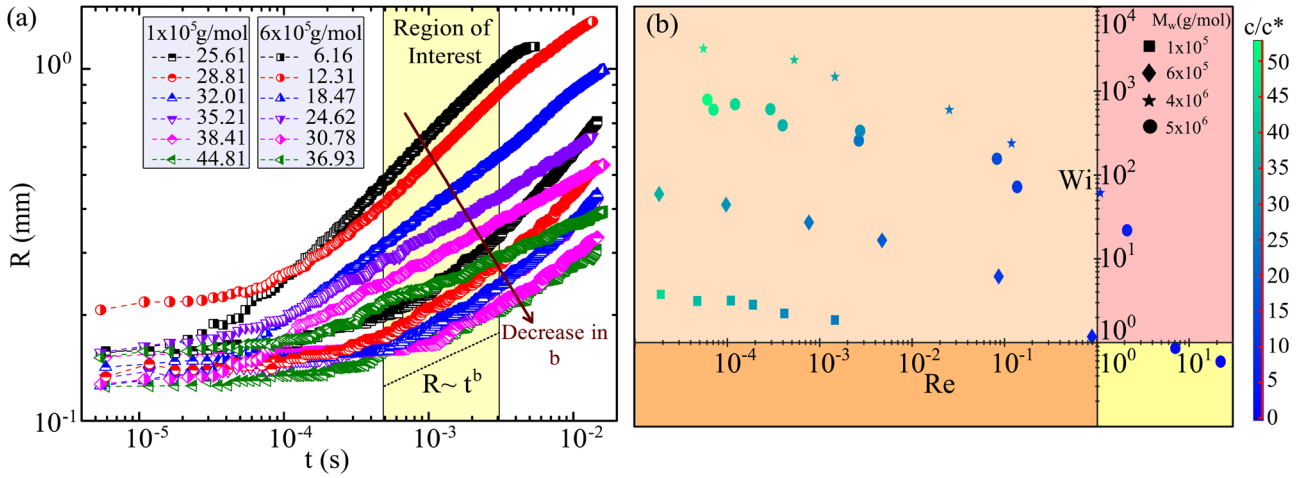

Fig. 5 (a) Growth in neck radius for various concentration ratios c/c^* of PEO solutions showing the decrease in slope b for $M_w = 1 \times 10^5$ g mol^{-1} and $M_w = 6 \times 10^5$ g mol^{-1}. (b) Regime map delineating coalescence regimes based on Re and Wi for a particular c/c^* across different molecular weights with (□) low Re/high Wi, (□) high Re/high Wi, (□) low Re/low Wi, and (□) high Re/low Wi regions (note: the data for $M_w = 4 \times 10^6$ and $M_w = 5 \times 10^6$ g mol^{-1} was obtained from our previous study[12]).

coalescence, the neck growth is driven by the influx of fluid towards the bridge from the nearby neighborhood region. Experimentally, the neck at the instant of the point of contact is less than the camera spatial resolution. So, a flat line is observed until a certain time instant, after which the growth of the neck begins. For a higher concentration ratio c/c^* solution this flat line is observed until 0.4 ms as observed in Fig. 5(a). Hence, we considered the lower limit of ROI as 0.5 ms. However, for lower c/c^* the neck growth starts at 0.1 ms. If the ROI for lower c/c^* is considered to start from less than 0.5 ms, there is no significant change in b value as shown in Fig. S3 (ESI†). The upper limit of ROI is determined on the basis of the characteristic time $T_c = \sqrt{\frac{R_0^2 \lambda \rho}{\eta_0}}$ which is $\sqrt{\lambda \times \tau_N}\left(\tau_N = \frac{\tau_i^2}{\tau_v}\right.$ in the Newtonian time scale, where τ_i is the inertial time scale and τ_v is the viscous time scale). The variation of T_c with c/c^* across molecular weights M_w is given in Fig. S4 (ESI†). It can be inferred from Fig. S4 (ESI†) that for lower c/c^*, $T_c \sim \mathcal{O}$ (10 ms), but at this time scale the coalescence process has already ended. Similarly, for higher c/c^*, $T_c \sim \mathcal{O}$ (1 ms). For consistency across various c/c^* of different M_w, we have chosen 3 ms as the upper limit for ROI. It should be noted that beyond 3 ms, for low c/c^*, the neck evolution is described by the significant vertical flow derived *via* gravity. For higher c/c^*, the shift in ROI beyond 3 ms (*i.e.* $t > T_c$) leads to a change in b, due to a decrease in $\mathrm{Wi}_i = \frac{\lambda U}{L}$, instantaneous Weissenberg number and increase in $\mathrm{Re}_i = \frac{\rho U L}{\eta_0}$, and instantaneous Reynolds number ($U \sim \partial R/\partial t$ and $L \sim R^2/2R_0$ are the characteristic scales associated with the flow) leading to transition from the elasticity dominated regime[12] to the viscoelastic regime[12] as shown in Fig. S5 (ESI†). However, the pure inertial dominant regime does not exist even for $\mathrm{Wi}_i \sim \mathcal{O}$ (10^{-3}–10^{-4}) as observed by Varma *et al.*[10] The change in ROI results in b tending toward the previously reported universal value[10,12] of 0.37.

Non-dimensional numbers

To interpret the neck evolution during coalescence of polymeric droplets it is essential to outline the underlying forces. These are elastic force F_e, viscous force F_v, inertial force F_i and capillary force F_c, where F_c drives the phenomenon while the other three resist it. The relative magnitudes of these resistive forces are captured by time averaged Reynolds number $\mathrm{Re} = \langle \mathrm{Re}_i \rangle$ and time averaged Weissenberg number $\mathrm{Wi} = \langle \mathrm{Wi}_i \rangle$. A regime map delineating coalescence regimes based on Re and Wi for a particular c/c^* is shown in Fig. 5(b). Four regimes are proposed on the basis of Re, Wi $> 10^0$ and Re, Wi $< 10^0$. It can be inferred from Fig. 5(b) that the solutions with $c/c^* > 20$ are in a low Re and high Wi regime. This regime is similar to the elasticity dominated regime ($c/c^* > 20$) proposed in our previous study.[12] Solutions in high Re, high/low Wi regimes are similar to the inertio-elastic regime.[12]

Scaling constants

In order to determine the closure to the analytical solution it is essential to study the physical behaviour of scaling parameters M_1, M_2 and M_3 represented in eqn (9). Here, M_1 is the coefficient of capillary force that drives the coalescence dynamics while M_2 and M_3 are the coefficients of axial stress τ_{rr} and shear stress τ_{rz} respectively that oppose neck growth. Owing to this nature, the coefficients M_2 and M_3 will have negative values while M_1 will have a positive value. The values of M_1, M_2 and M_3 are obtained by an iterative algorithm based on experimental data. The details of the algorithm are shown in Fig. S6 (ESI†). The obtained values of M_1 with c/c^* with delineation based on the regimes proposed in our previous study[12] (inertio-elastic (IE), viscoelastic (VE) and elasticity dominated (ED) regimes) is

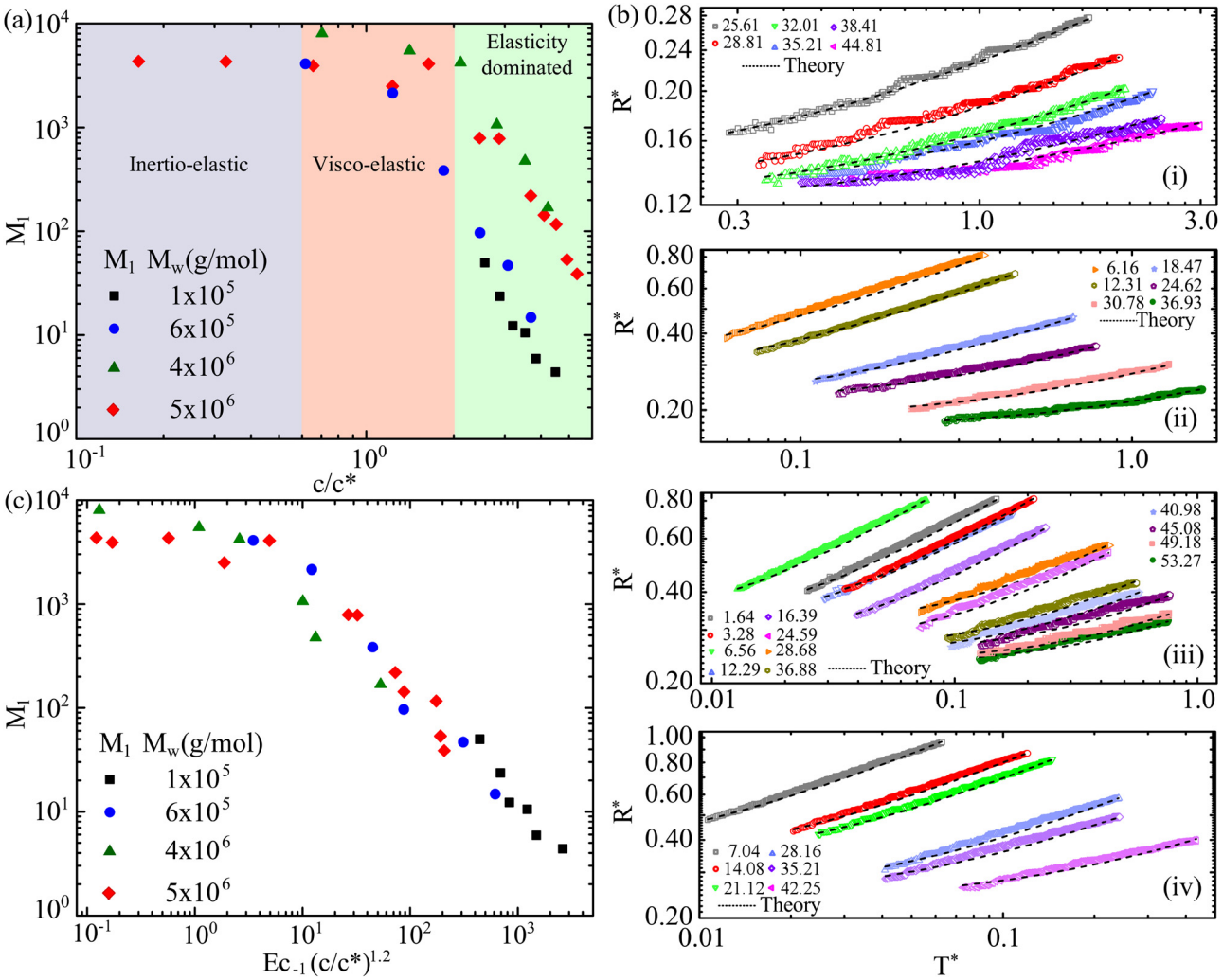

Fig. 6 (a) Dependence of scaling constant M_1 on c/c^* for various molecular weights across various regimes, namely, inertio-elastic, visco-elastic and elasticity dominated regimes. (b) Agreement between the experiments and solution of eqn (10) for various c/c^* of (i) $M_w = 1 \times 10^5$ g mol^{-1}, (ii) $M_w = 6 \times 10^5$ g mol^{-1}, (iii) $M_w = 5 \times 10^6$ g mol^{-1}, and (iv) $M_w = 4 \times 10^6$ g mol^{-1} (data for (iii) and (iv) was obtained from Varma *et al.*[12]). (c) Collapse of data for M_1 across molecular weights representing the dependence on Ec_{-1} in which c/c^* is added empirically.

represented in Fig. 6(a). It is constant in IE and VE followed by a monotonic decrease in ED.

Once the value of M_1 is obtained, the values of M_2 and M_3 are determined by repeating the same algorithm chronologically by keeping M_1 constant. It is observed that the theoretical solution determined from eqn (11) has a strong dependence on M_1 which is intuitive as it corresponds to the relative magnitude of capillary and elastic forces. The values of M_2 and M_3 are of the same order $\mathcal{O}(10^2)$ and have a weak effect on the theoretical solution and therefore in the present study they have been assumed constant as $M_2 = M_3 = -100$. Even though M_2 is the scaling constant for elastic force, this weakly influences the theoretical solution as the effect of elastic stresses are absorbed by M_1. Similarly, the effect of M_3 is negligible as it is the scaling constant of viscous force.

The neck evolution represented in the ROI of Fig. 5(a) is non-dimensionalized with drop radius R_0 and time with T_c. This dimensionless neck radius $R^* = R/R_0$ with dimensionless time $T^* = t/T_c$ is represented in Fig. 6(b) along with the numerical solution proposed by eqn (11) using the values of M_1 given in Fig. 6(a). Fig. 6(b) shows the good agreement between the experiments and the proposed theory for $M_w = 1 \times 10^5$ g mol^{-1}, $M_w = 6 \times 10^5$ g mol^{-1}, $M_w = 5 \times 10^6$ g mol^{-1} (obtained from Varma *et al.*[12]), and $M_w = 4 \times 10^6$ g mol^{-1} (obtained from Varma *et al.*[12]) respectively. The power-law exponent b obtained by fitting the experimental and the numerical data are given in Table 1 as b and b_{theo} respectively where b_{theo} is the power-law exponent obtained from the fitting of theoretical data.

The scaling constant M_1 has a strong dependence on the inverse of Elasto-capillary number $Ec_{-1} = \frac{\text{Elastic Force}}{\text{Capillary Force}} = \frac{\eta_0 R_0}{\sigma\lambda}$ as shown in Fig. S7(a) (ESI†). Based on this dependence $c/c^{*1.2}$ is added empirically to unify the functional form over different molecular weights as represented in Fig. 6(c). It is

observed numerically that b_{theo} has strong dependence on M_1. This is expected as M_1 in eqn (9) corresponds to the relative contributions of capillary forces during the neck growth. It has been observed from of our previous experiments[12] that, as the elasticity of droplets increases, the curvature of the neck formed during coalescence changes, leading to an increase in capillary forces. Therefore, the term corresponding to M_1 in eqn (9) increases in magnitude. In order to maintain an overall balance in eqn (9), the coefficient M_1 decreases. As M_1 needs to account for the relative magnitude of capillary and elastic forces, it has a strong functional dependence on Ec_{-1} which can be observed in Fig. 6(c). It can be noted from Fig. 6(c) that M_1 has a nearly constant value until $Ec_{-1}(c/c^*)^{1.2} \sim O(10^1)$ and then it decreases as the elastic forces increase. This is also the signature of the presence of three different regimes in coalescence where the exponent b is constant in the IE/VE regime and a function of relaxation time λ in the ED regime.[12]

In order to use the theory for unknown fluids, first the scaling constant M_1 needs to be determined. M_1 is obtained by first determining $Ec_{-1}(c/c^*)^{1.2}$ and then interpolating based on the nearest values from Fig. 6(c). To check this, the theoretical solution for various c/c^* of Polyacrylamide (PAM) (data acquired from our previous study[10]) is obtained. This theoretical solution is in good agreement with the experimental data and the same is shown in Fig. S8 (ESI†). It is important to note that the theory holds good for $Wi_c > 1$. However, the theory can be extended to the boundary region of $Wi_c \sim \mathcal{O}(10^{-1})$ with a saturation value of $M_1 = 8000$ as observed from Fig. 6(c).

Sub-Newtonian coalescence

The power-law exponent b is the signature of the dominant governing force in coalescence dynamics. Apart from the early time scale where the exponent value is unity, it has a regime-dependent value for later time scales. For Newtonian, it has a universal value of $b = 0.5$,[28–30] while for polymeric droplets, it is $b \leq 0.38$.[10] This reduction in evolution exponent results from the sluggish merging of the two polymeric droplets. The idea of sub-Newtonian is defined on the basis of power law exponent b which is less than 0.5 (inertial regime of Newtonian droplet coalescence) in analogy to the slowed diffusion of Brownian particles in viscoelastic media where the diffusive exponent α less than unity in $\langle \Delta r^2 \rangle \propto t^{\alpha}$ marks the sub-diffusive regime.[31] The force balance in the coalescence phenomenon is $F_c \sim F_v + F_i + F_o$, where F_v and F_i are viscous and inertial forces respectively while F_o is an additional opposing force caused due to various mechanisms. One such mechanism is fluid elasticity caused by macromolecular chains which causes the elastic force $F_o = F_e$ to slow down the neck growth. This elastic force resulting from solid-like behaviour can also originate from rearrangement of magnetic and conductive particles under the influence of magnetic and electric fields respectively, in Magento rheological fluids (MRFs) and Electro rheological fluids (ERFs). Another mechanism which can hinder the neck growth is the difference in surface tensions between two immiscible droplets leading to $F_o = f(\sigma_{pendant} - \sigma_{sessile}, \kappa)$ (κ is curvature) as shown by Xu *et al.*[15] Recently, Kulkarni *et al.*[32] showed the existence of an intermediate regime between partial and complete coalescence in immiscible oil–water systems. For Newtonian miscible droplets coalescence, $F_o = 0$ leads to $b = 1$ or 0.5. In summary, sub-Newtonian coalescence is due to the result of non-zero F_o which can happen in both Newtonian and non-Newtonian droplet coalescence.

The scaling based mathematical representation of the coalescence behaviour is given as follows:

$$U^2 \sim \phi(\chi, R, R_0) + \delta(\chi, R, R_0, U^n) \quad (12)$$

Here, U^2 is the scale of inertia potential, ϕ is the capillary potential, and δ is the material potential with χ, a function of material properties and n is the coalescence index. For Newtonian fluids, $n = 1$ and $\chi = \alpha(\eta, \sigma, \rho)$ leads to an equation proposed by Xia *et al.*[30] However, for polymer solutions which we classify as an example of sub-Newtonian coalescence, $n = -2$ and $\chi = \alpha(\eta, \lambda, \sigma, \rho)$ resulting in a bi-quadratic equation as eqn (10). For other classes of materials which can potentially give sub-Newtonian behaviour, χ and n need to be defined in eqn (12) according to the material. For instance χ for immiscible Newtonian droplet coalescence includes the surface tension difference *i.e.* $\sigma_{pendant} - \sigma_{sessile}$.

Macromolecular description

Our previous study on sub-Newtonian type coalescence[12] showed power-law exponent b depends on $\tau^* = \sqrt{\frac{\eta_0 \lambda}{\rho R_0^2}}$ (ratio of relaxation time and the Newtonian time scale). The corresponding dependence of b for $M_w = 6 \times 10^5$ and $M_w = 1 \times 10^5$ g mol^{-1} along with the data obtained from our previous study[12] for $M_w = 5 \times 10^6$ g mol^{-1} and $M_w = 4 \times 10^6$ g mol^{-1} is shown in Fig. 7(a). It is observed that there is a significant deviation in b *vs.* τ^* for $M_w = 6 \times 10^5$ and $M_w = 1 \times 10^5$ g mol^{-1} compared to the other two molecular weights. This deviation is related to the macromolecular dynamics of the chains rather than the continuum behaviour. This dependence can be explained using the entanglement density *i.e.* entanglement junctions per chain, $N_e = \left(\frac{M_w}{M_e}\right)\left(\frac{c}{c^*}\right)$,[33] where M_e is the entanglement molecular weight, which is 2000 g mol^{-1} for PEO.[34] The N_e values for different c/c^* and M_w are given in Fig. 7(c). It can be observed from Fig. 7(c) that the entanglement densities for the same c/c^* across the molecular weights differ by an order between $M_w = 1 \times 10^5$, 6×10^5 g mol^{-1} and 5×10^6 g mol^{-1}. Whereas, for molecular weights of 4×10^6 g mol^{-1} and 5×10^6 g mol^{-1}, N_e is of the same order. As N_e for $M_w = 1 \times 10^5$ and $M_w = 6 \times 10^5$ g mol^{-1} is less than the other two molecular weights, the chains have lesser topological constraints owing to the small chain lengths resulting in much lower relaxation times. The corresponding entanglement constraints for two different chain lengths is represented in Fig. 7(b) as a schematic. This difference in relaxation times is reflected in the continuum approach through the shear modulus $G = \eta_0/\lambda$. The G values corresponding to various c/c^* and M_w are given in Table 1. The difference in G for the same c/c^* across the

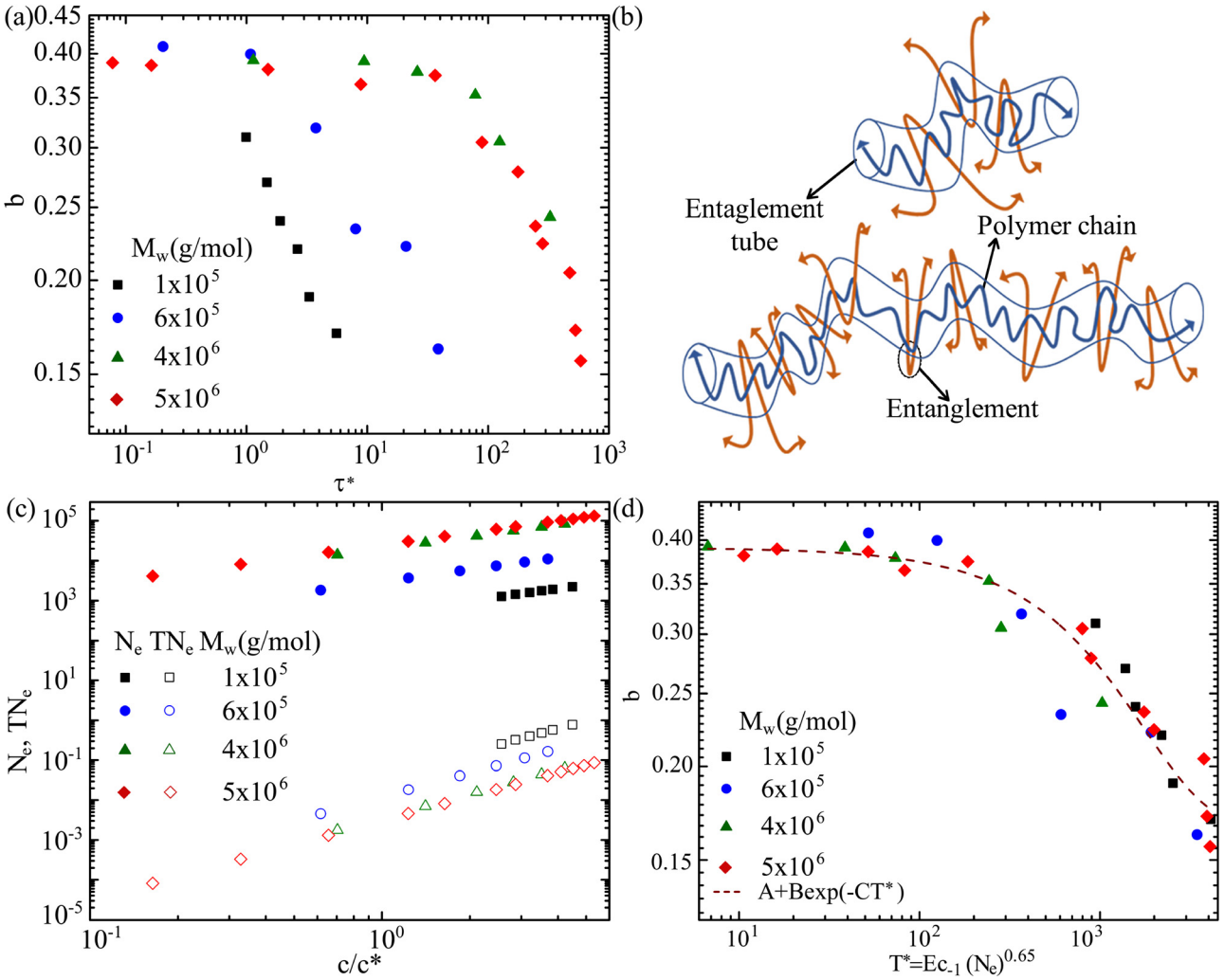

Fig. 7 (a) Variation of b with the dimensionless time τ^* proposed in our previous study[12] across different molecular weights. (b) Schematic of the chain entanglements for two different chain lengths. (c) Dependence of entanglement density N_e and total entanglement density $TN_e = N_e \times N_d$ (N_d is the order of number of chains) on c/c^* across molecular weights and (d) dependence of the power-law exponent b on T^* (ratio of τ_v and relaxation time λ) for various molecular weights. The dashed line represents the exponential fit of 94% confidence interval with $A = 0.1653 \pm 0.01532$, $B = 0.22545 \pm 0.01508$, and $C = 0.00076 \pm 0.00017$.

molecular weights suggests a stronger approach to solid-like behaviour leading to a faster decrease in exponent b for $M_w = 1 \times 10^5$ and $M_w = 6 \times 10^5$ g mol^{-1}. This is further understood by the scale of total entanglement density $TN_e = N_e \times N_d$ where N_d is the scale of the number of chains per unit volume. Fig. 7(c) shows that for the same c/c^*, TN_e increases as the M_w decreases indicating a higher density of entanglement junctions per unit volume for lower M_w resulting in higher G at the same c/c^*. As the coalescence process is an energy minimization phenomenon, the increase in G leads to an increase in elastic energy per unit volume[35] $e = \frac{3}{2}G\varepsilon^2$. Once this elastic energy predominates the surface energy, the coalescence is arrested. This approach to arrested coalescence leads to a faster decrease in b.

To account for the deviation of b with τ^* (and b with Ec_{-1} shown in Fig. S7(b), ESI†) across molecular weights as represented in Fig. 7(a), we redefine the non-dimensional characteristic time as $T^* = \frac{\tau_v}{\lambda}(N_e)^{0.65} = Ec_{-1}(N_e)^{0.65}$ (where, $\tau_v = \frac{\eta_0 R_0}{\sigma}$). Here, $N_e{}^{0.65}$ is added empirically to obtain a collapse in data across molecular weights. This term accounts for the entanglement density which is the fingerprint of entanglement junctions in the continuum. Therefore, $T^* = Ec_{-1}(N_e)^{0.65}$ is the corrected time scale to represent the behaviour of power-law exponent b. This behaviour is represented in Fig. 7(d). Incorporating N_e in T^* suggests that the continuum approach is not complete until the molecular description of chain dynamics *via* entanglement densities are empirically added to the continuum description. Similarly, c/c^* was empirically added in the functional dependence of the scaling constant M_1 with Ec_{-1} to account for the entanglement densities. The collapse of data shown in Fig. 7(d) follows an exponential decay function similar to that in our previous study.[12]

Arrested coalescence

Finally, we look at one of the limiting cases of eqn (11). For getting a physically acceptable solution, it is important to have a non-negative sum under square-root. One such case that violates the condition is when $P = 0$ as the term M_2 is always negative. On substituting $P = 0$, we obtain eqn (13) that can be further simplified to obtain a cut-off radius in terms of material properties at which the coalescence is arrested.[36] As observed from Table 1, the value of the term $|-\frac{M_1}{M_2}|$ is bounded by $\mathcal{O}(10)/\mathrm{Ec}_{-1}$. Under small angle limit $R^* = \theta$ as represented in Fig. S9 (ESI†), eqn (13) is further simplified to obtain the θ_{arrest} (angle subtended by the neck when coalescence is arrested) as represented in eqn (14) (see the ESI† for the intermediate steps).

$$-M_1 = \frac{M_2\left(1+\frac{2}{\mathrm{Wi_c}}\right)}{\frac{1}{R^*}+\frac{2}{(R^*)^2}} \tag{13}$$

$$\theta_{\mathrm{arrest}} = \frac{4.47}{\sqrt{\mathrm{Ec}_{-1}}} \tag{14}$$

The proposed value for θ_{arrest} is in good agreement with the value proposed in the literature for high elasticity droplets.[37] To further validate θ_{arrest} given in eqn (14), experiments are performed on $c/c^* = 70$ of $M_w = 1 \times 10^5$ g mol^{-1} having the properties $\eta_0 = 54$ Pa s and $\lambda = 14$ ms. The snapshots showing the neck at $t = 0$ s and $t = 1$ s are shown in Fig. 8(a) and (b) respectively. In the current study, we have considered coalescence as arrested if $\dot{\gamma}_{\mathrm{arrest}} < 0.5\%(\dot{\gamma}_{\mathrm{DIwater}})$, where $\dot{\gamma}$ is the shear rate (see the ESI† for shear rate calculations). The value of θ_{arrest} obtained from the experiments is 0.56 radians which is in agreement with the value obtained from eqn (14) *i.e.* 0.52 radians. This experimentally obtained θ_{arrest} is closer to the value obtained from eqn (14) than to the value obtained from the relationship proposed by Ongenae *et al.*[37] for the arrested coalescence. However, it is important to note that in the sessile-pendant configuration, gravity becomes an important parameter at higher time scales owing to which coalescence is no longer arrested.

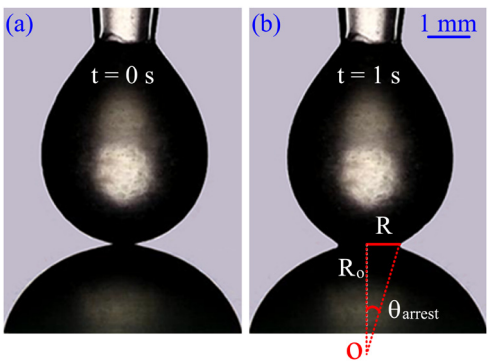

Fig. 8 Snapshots showing the neck at (a) $t = 0$ s and (b) $t = 1$ s representing the arrested coalescence for $c/c^* = 70$ of $M_w = 1 \times 10^5$ g mol^{-1}.

Triggering mechanisms for coalescence

The neck evolution dynamics, as discussed in previous subsections, is the signature of dominant forces. These dominant forces depend on the method by which coalescence is triggered. In the present study and our previous studies,[10,12] we fix the volume of the drops and bring one drop towards the other drop with negligible approach velocity (Weber number We $\sim$ 0). Dekker *et al.*[20] use the volume-filling approach, where the fluid is pumped continuously until the drops touch each other, resulting in an additional inertial effect. This inertial effect is particularly predominant at the early time scales. A schematic of the two methods is shown in Fig. 9. The effect of different triggering mechanisms is explained by Varma *et al.*[13] for the case of two sessile drops coalescence. However, a detailed study needs to be carried out on the sessile-pendant configuration. Dekker *et al.*[20] have reported the value $b = 0.5$ for polymeric solutions, which contrasts the sub-Newtonian value $b < 0.5$. This discrepancy is attributed to polymer relaxations. In order to stretch the polymer chains, it is not only essential to have high strain rates but also accumulations of strains.[38,39] This indicates that polymeric fluids may behave as Newtonian fluids if the strains are smaller at early time scales. For coalescence, such observations are reported by Chen *et al.*,[14] which is also reported by Dekker *et al.*[20] However, our discussion is for a later timescale where the elasticity effects are predominant.

Coalescence *vs.* pinch off of polymer solutions

Singular events like pinch-off and coalescence have two important properties: scale invariance and universality.[40] Scale invariance

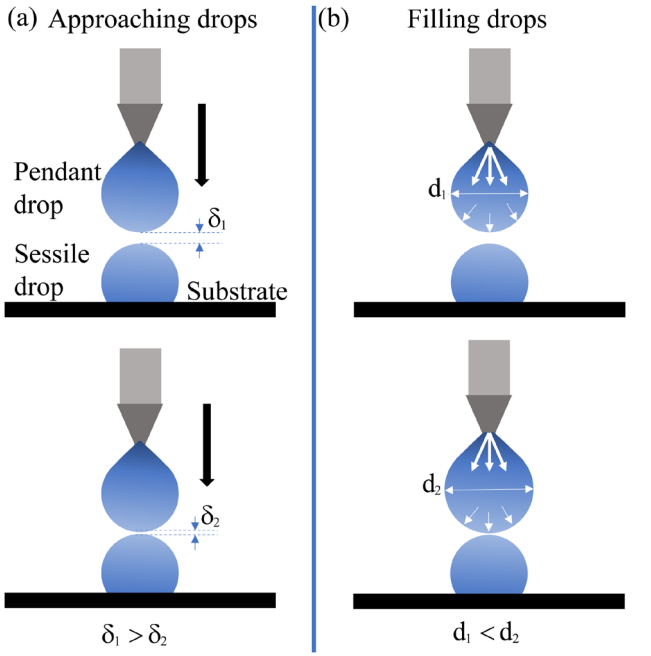

Fig. 9 Schematic of different methods for achieving coalescence in sessile pendant geometry. (a) Approaching drops: one drop approaches the other at negligible velocity. (b) Filling drops: the volume of one drop is increased to eventually coalesce with the other drop.

implies that the change of scale in the neck radius R can be absorbed into the change of time scale, leading to the same power law. A universality property implies the structure is insensitive to initial conditions or other aspects of the large-scale structures of the solution. In a sense, the two events are an inverse of each other, *i.e.*, in pinch-off, the capillary thinning of neck radius R precedes the singularity, while in coalescence, the singularity precedes the bridge evolution that later evolves in time. Owing to this, unlike pinch-off, coalescence always has a power law behaviour. Pinch-off in polymers is known to show a capillary thinning regime which is the signature of fluid elasticity under extensional flows. It has exponential[41] characteristics in the Elastocapillary (EC) regime and power-law behaviour[42] in the Terminal viscoelastocapillary (TVEC) regime. In unentangled polymer solutions, EC is pronounced compared to TVEC; for entangled polymer solutions, TVEC is predominant. The thinning is more distinct[42] for fluids with a higher relaxation time λ than those for smaller relaxation time fluids. This thinning which is of the form[41] $R \sim \exp(-t/3\lambda)$ for unentangled polymers, is sluggish for fluids with higher relaxation times. Our study for the power law exponent b shows a similar trend. For a fixed molecular weight M_w, the fluids with higher λ have smaller b, *i.e.*, the neck radius $R \sim t^b$ evolves sluggishly and *vice versa*. However, across different molecular weights, λ alone is not a sufficient parameter, and microscopic parameters like the entanglement density N_e are required to understand the overall trend.

5. Summary

In the current work, we have developed a theoretical framework to model polymeric droplet coalescence. We have unified the various constitutive laws under a high Weissenberg creep flow limit to obtain a scaling-based neck evolution equation. The theoretical framework is validated across different molecular weights of poly(ethylene oxide) (PEO) with experiments. Our experiments and theoretical models have both highlighted the importance of macromolecular parameters for understanding the coalescence dynamics. The study also reports an empirically corrected T^* over our previous study to account for entanglement densities across different molecular weights. The theoretical framework is further validated by looking at a limiting case of arrested coalescence under a small angle limit. The value we obtain for θ_{arrest} is found to be inversely proportional to $Ec_{-1}^{1/2}$ and is validated with experiments along with the value proposed in the literature. Finally, we name the coalescence as sub-Newtonian if $b < 0.5$ with limiting case $b \to 0$ as arrested. However, the current framework implicitly assumes Weber Number $We = (\rho U_{approach}^2 R_0)/\sigma \to 0$ (where $U_{approach}$ is the relative approach velocity between the two drops) and neglects the effect of surrounding fluids by assuming a low approach velocity and air as the outer fluid, respectively. Further studies on different complex fluids are required to broaden the class of sub-Newtonian coalescence along with the effect of higher approach velocities and different surrounding fluids to explore the extremes of three other regimes proposed by Fig. 5(b). It also poses an open question about the existence of Super-Newtonian coalescence $b > 0.5$ where the merging dynamics will be driven by an additional force other than capillary and therefore will hasten the coalescence dynamics.

Conflicts of interest

There are no conflicts to declare.

Acknowledgements

We acknowledge partial funding support from DST SERB India: CRG/2022/005381.

Notes and references

1 J. Frenkel, *J. phys.*, 1945, **9**, 385.
2 E. Villermaux and B. Bossa, *Nat. Phys.*, 2009, **5**, 697.
3 H. R. Pruppacher and J. D. Klett, *Microphysics of Clouds and Precipitation*, Springer, 2010, pp. 10–73.
4 M. Orme, *Prog. Energy Combust. Sci.*, 1997, **23**, 65–79.
5 T. Hopfes, J. Petersen, Z. Wang, M. Giglmaier and N. Adams, *Int. J. Multiphase Flow*, 2021, **143**, 103723.
6 S. Stewart and G. Mazza, *J. Food Qual.*, 2000, **23**, 373–390.
7 N. Ashgriz and J. Poo, *J. Fluid Mech.*, 1990, **221**, 183–204.
8 H. Djohari, J. I. Martnez-Herrera and J. J. Derby, *Chem. Eng. Sci.*, 2009, **64**, 3799–3809.
9 J. Ambrose, M. Livitz, D. Wessels, S. Kuhl, D. F. Lusche, A. Scherer, E. Voss and D. R. Soll, *Am. J. Cancer Res.*, 2015, **5**, 3485.
10 S. C. Varma, A. Saha, S. Mukherjee, A. Bandopadhyay, A. Kumar and S. Chakraborty, *Soft Matter*, 2020, **16**, 10921–10927.
11 S. C. Varma, A. Saha and A. Kumar, *Phys. Fluids*, 2021, **33**, 123101.
12 S. C. Varma, A. S. Rajput and A. Kumar, *Macromolecules*, 2022, **55**, 6031–6039.
13 S. C. Varma, D. Dasgupta and A. Kumar, *Phys. Fluids*, 2022, **34**, 093112.
14 S. Chen, E. Pirhadi and X. Yong, *J. Colloid Interface Sci.*, 2022, **618**, 283–289.
15 H. Xu, T. Wang and Z. Che, *J. Colloid Interface Sci.*, 2022, **628**, 869–877.
16 H. Chen, X. Pan, Q. Nie, Q. Ma, H. Fang and Z. Yin, *Phys. Fluids*, 2022, **34**, 032109.
17 N. P. Thien and R. I. Tanner, *J. Non-Newtonian Fluid Mech.*, 1977, **2**, 353–365.
18 N. Phan-Thien, *J. Rheol.*, 1978, **22**, 259–283.
19 M. A. Fardin, M. Hautefeuille and V. Sharma, *Soft Matter*, 2022, **18**, 3291–3303.
20 P. J. Dekker, M. A. Hack, W. Tewes, C. Datt, A. Bouillant and J. H. Snoeijer, *Phys. Rev. Lett.*, 2022, **128**, 028004.
21 R. B. Bird, R. C. Armstrong and O. Hassager, *Dynamics of polymeric liquids, vol. 1: Fluid mechanics*, Wiley, 2nd edn, 1987.

22 H. Giesekus, *J. Non-Newtonian Fluid Mech.*, 1982, **11**, 69–109.
23 M. Renardy, *J. Non-Newtonian Fluid Mech.*, 1997, **69**, 293–301.
24 N. D. Polychronopoulos, L. T. Benos, C. I. Stergiou, I. E. Sarris and J. Vlachopoulos, *Soft Matter*, 2022, **18**, 4017–4029.
25 C. T. Bellehumeur, M. Kontopoulou and J. Vlachopoulos, *Rheol. Acta*, 1998, **37**, 270–278.
26 O. Arnolds, H. Buggisch, D. Sachsenheimer and N. Willenbacher, *Rheol. Acta*, 2010, **49**, 1207–1217.
27 V. Tirtaatmadja, G. H. McKinley and J. J. Cooper-White, *Phys. Fluids*, 2006, **18**, 043101.
28 M. Wu, T. Cubaud and C.-M. Ho, *Phys. Fluids*, 2004, **16**, L51–L54.
29 J. D. Paulsen, J. C. Burton and S. R. Nagel, *Phys. Rev. Lett.*, 2011, **106**, 114501.
30 X. Xia, C. He and P. Zhang, *Proc. Natl. Acad. Sci. U. S. A.*, 2019, **116**, 23467–23472.
31 J. Sprakel, J. van der Gucht, M. A. C. Stuart and N. A. Besseling, *Phy. Rev. E*, 2008, **77**, 061502.
32 V. Kulkarni, V. Y. Lolla, S. R. Tamvada, N. Shirdade and S. Anand, *J. Colloid Interface Sci.*, 2021, **586**, 257–268.
33 Q. Huang, O. Mednova, H. K. Rasmussen, N. J. Alvarez, A. L. Skov, K. Almdal and O. Hassager, *Macromolecules*, 2013, **46**, 5026–5035.
34 P. Nath, R. Mangal, F. Kohle, S. Choudhury, S. Narayanan, U. Wiesner and L. A. Archer, *Langmuir*, 2018, **34**, 241–249.
35 A. B. Pawar, M. Caggioni, R. W. Hartel and P. T. Spicer, *Faraday Discuss.*, 2012, **158**, 341–350.
36 A. B. Pawar, M. Caggioni, R. Ergun, R. W. Hartel and P. T. Spicer, *Soft Matter*, 2011, **7**, 7710–7716.
37 S. Ongenae, M. Cuvelier, J. Vangheel, H. Ramon and B. Smeets, *Front. Phys.*, 2021, 321.
38 D. Bousfield, R. Keunings, G. Marrucci and M. Denn, *J. Non-Newtonian Fluid Mech.*, 1986, **21**, 79–97.
39 N. K. Chandra, S. Sharma, S. Basu and A. Kumar, arXiv, 2022, preprint, arXiv:2205.15597.
40 J. Eggers and M. A. Fontelos, *Singularities: Formation, Structure, and Propagation*, Cambridge University Press, 2015.
41 J. Dinic and V. Sharma, *Proc. Natl. Acad. Sci. U. S. A.*, 2019, **116**, 8766–8774.
42 J. Dinic and V. Sharma, *Macromolecules*, 2020, **53**, 3424–3437.

